Supporting Information

# Scalable and Resilient Etched Metallic Micro- and Nano-Structured Surfaces for Enhanced Flow Boiling

Nithin Vinod Upot[1], Allison Mahvi[1,2†], Kazi Fazle Rabbi[1†], Jiaqi Li[1], Anthony M. Jacobi[1*], Nenad Miljkovic[1,3,4,5*]

([†]Equal Contribution, *Corresponding Authors)

[1]Department of Mechanical Science and Engineering, University of Illinois at Urbana-Champaign, Urbana, IL, 61801, USA
[2]Current Address: National Renewable Energy Laboratory, Golden, CO, 15013, USA
[3]Materials Research Laboratory, University of Illinois at Urbana–Champaign, Urbana, Illinois 61801, USA
[4]Department of Electrical and Computer Engineering, University of Illinois, Urbana, Illinois 61801, United States
[5]International Institute for Carbon Neutral Energy Research (WPI-I2CNER), Kyushu University, 744 Moto-oka, Nishi-ku, Fukuoka, 819-0395, Japan

E-mail: a-jacobi@illinois.edu, nmiljkov@illinois.edu

## S1. Fabrication Materials

CAS numbers of chemicals used in the formation of internal etched aluminum and boehmite structures are mentioned in Table S1.

**Table S1.** Sigma-Aldrich CAS Numbers.

| Chemical | CAS Number |
|---|---|
| Acetone | 67-64-1 |
| Ethanol | 64-17-5 |
| Deionized water | 7732-18-5 |
| HCl | 7647-01-0 |

## S2. Video - Flow Visualization

**Video S1**. Flow regime visualization at test-section exit. This video captures stratified and annular flow regimes at test-section exit for the low and high mass flux cases. This video is captured with a Phantom high speed camera at 5000 fps, and enhanced turbulence with the microstructured surface is clearly visible.

## S3. Characterization

**XPS:** X-ray photoelectron spectroscopy (XPS) data was obtained using a Kratos Analytical Axis Ultra with a monochromatic Al Kα X-ray source. The size of the source beam was 2 mm × 2 mm, and the size of the analyzed region was 0.3 mm × 0.7 mm. The instrument was maintained at a pressure of $10^{-7}$ Pa during the experiments. The spectra were post processed with Casa XPS software (Casa Software Ltd.).

**Confocal Microscopy:** Keyence VK-X1000 3D Laser Scanning Confocal Microscope was used to obtain the confocal microscopy images.

**AFM:** Asylum Research MFP-3D and Anton Paar Tosca 400 Atomic Force Microscopes were used to obtain the atomic force microscopy images.

**SEM/FIB:** Hitachi S-4800 Scanning Electron Microscope was used to obtain the regular SEM images. The cross-sectional SEM images were taken with Thermo Scios2 Dual-Beam SEM/FIB.

## S4. Test Section

The test section is a 0.83 m long, 3.048 mm diameter aluminum tube that is wrapped with a 700 W rope heater that acts as the heat source. The test section surface heat flux is controlled with a DC power supply through LabVIEW. Absolute pressure transducers are used at the inlet to the preheater and test-section while a differential pressure transducer is used to measure the pressure drop across the test section. T-type thermocouple probes are placed at the inlet and exit of the preheater and two RTD's are placed at the inlet and exit of the test section. Twelve fine-gauge K-type thermocouples are placed along the test section at six locations to measure the local wall temperatures. Each location has two wall thermocouples affixed at the top and bottom of the tube. The calibrated thermocouples were placed in machined slots and attached to the tube with copper tape and a thermally conductive paste. A glass tube of the same diameter as that of the test section was placed at the exit of the test section to record flow regimes as the refrigerant leaves the test section.

Subcooled refrigerant leaving the preheater enters the test section, where the heat supplied is incremented in small amounts keeping operating parameters like mass flux and saturation pressure constant. Heat flux is increased in this manner till dry-out occurs. This two-phase refrigerant is then condensed and enters back into the pump after which the cycle repeats. No fluctuations in temperature and pressure across the test-section were observed for the range of tests conducted. Flow regimes are recorded at 5000 FPS using a Phantom high-speed camera with a 50 W light source placed normal to the visualization section. Heat transfer coefficients of structured tubing is compared to the baseline plain metallic tubing with the convective thermal resistance dominating over the radial conductive thermal resistance. The experimental operating conditions across the test section are presented in Table S2.

**Table S2:** Operating conditions of R134a in the test section.

| Parameter | Value |
|---|---|
| Heat Flux ($kW/m^2$) | 0.5-55 |
| Mass Flux ($kg/m^2s$) | 100-300 |
| Saturation Pressure (kPa) | 760 |
| Length (m) | 0.83 |
| Diameter (mm) | 3.048 |
| Test Section Material | Aluminum |

Local heat transfer coefficients across the test section are determined and compared for a variety of operation conditions such as heat flux, mass flux and saturation pressure for both plain and etched tubes. Comparisons of average heat transfer coefficients and pressure drop are also reported.

## S5. Data Reduction

The total power supplied to the test section is calculated through knowledge of the voltage and current output of the DC power supply.

$$Q = V.I \tag{S1}$$

Using the heat flux and the distance between adjacent wall thermocouples, the enthalpy at each thermocouple location was calculated with an energy balance

$$q''\pi D(z_i - z_{i-1}) = \dot{m}(h_i - h_{i-1}) \tag{S2}$$

where $q''$ represents the test-section heat flux taking into account ambient losses, $z_i$ represents the axial location of the thermocouple and the inlet condition ($h_0$) is known based on the temperature and pressure at the test section inlet. The local quality can then be calculated with the local enthalpy and pressure. The pressure at each location was estimated assuming a linear pressure drop between the inlet and outlet. The total measured pressure drop includes the pressure loss in the test section and the visualization section. The pressure drop across the test section was isolated by removing the contributions from the visualization section and the expansions and contractions in the fittings (estimated using minor loss coefficients for expansion and contraction).[1, 2] Reported pressure drops in this paper are given according to equation 3:-

$$\Delta P_{TS} = \Delta P_{meas} - \phi_{lo}^2 \left(\frac{2 f_{lo} G_{vis}^2}{\rho_l D_{vis}}\right) L_{vis} - \Delta P_{minor} \tag{S3}$$

where ϕ refers to the two-phase frictional multiplier, f is the friction factor and G is the mass flux. Subscripts ‘lo’ refers to liquid-only and ‘vis’ refers to the visualization section.

The local pressure at each thermocouple location along the tube is determined through a linear pressure drop assumption across the tube length. Finally, the local heat transfer coefficient can be

calculated with the local refrigerant ($T_{ref}$) and wall ($T_w$) temperatures, as shown in equation 4. The calculation accounts for both the convective resistance and the thermal resistance through the wall.

$$htc_i = \left[ \frac{T_{w,i} - T_{ref,i}}{q''} - \frac{r_{in} \ln\left(\frac{r_{out}}{r_{in}}\right)}{k} \right]^{-1} \quad \text{(S4)}$$

The average heat transfer coefficient across the test section is then calculated as the mean value of local heat transfer coefficients. All data analysis and uncertainty propagation are performed using Engineering Equation Solver (EES). Uncertainties of measured variables are presented in Table S3.

**Table S3.** Details of instrumentation on the test facility and the uncertainty for each measurement.

| Measurement | Instrument | Locations | Span | Uncertainty |
|---|---|---|---|---|
| Refrigerant Temperature | T-Type Thermocouple | Pre-Heater Inlet, Pre-Heater Outlet | 0 to 100°C | ±0.25°C |
| Refrigerant Temperature | RTD | Test Section Inlet, Test Section Outlet | 0 to 100°C | ±0.1°C |
| Absolute Pressure | Piezoresistive Transducer | Pre-Heater Inlet | 0 to 6900 kPa | ±5.5 kPa |
| Absolute Pressure | Piezoresistive Transducer | Test Section Outlet | 0 to 3450 kPa | ±2.8 kPa |
| Pressure Drop | Differential Pressure Transducer | Across Test Section | 0 to 50 kPa | ±0.2 kPa |
| Flow Rate | Coriolis Sensor | Pre-Heater Inlet | 35 to 1600 g $min^{-1}$ | ±0.10% |
| Wall Temperatures | K-Type Thermocouple | Test Section | 0 to 100°C | ±0.25°C |

## S6. Facility Validation

Single-phase validation tests were performed over a range of test-conditions, and heat transfer coefficient results were compared with expected values based on the Gnielinski correlation.[3]

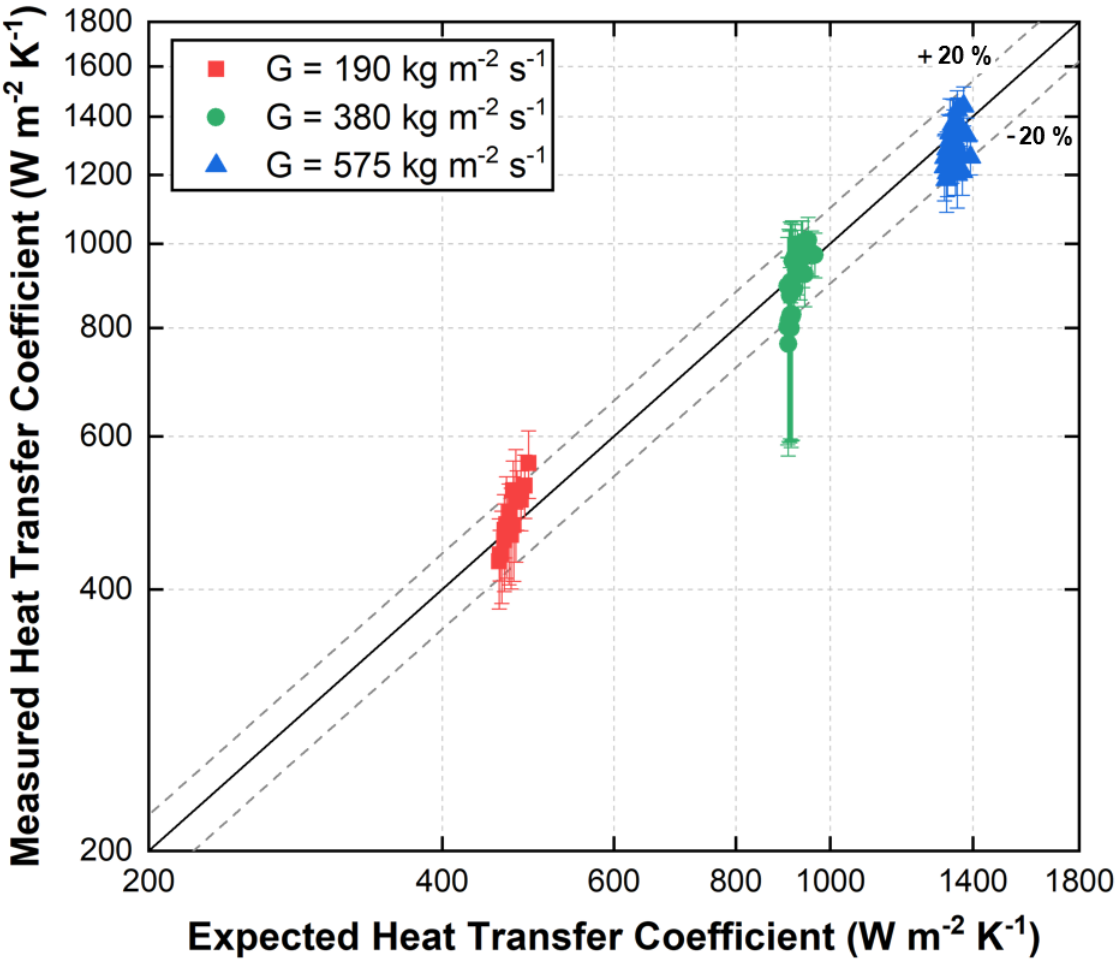


**Figure S1.** Comparison of experimental single-phase heat transfer coefficients with expected heat transfer coefficients

Experimental heat transfer coefficient results are within 20% of the predicted values, thereby validating the facility.

## S7. Heat Flux vs Wall Superheat Curves

Figure S2 shows the variation of heat flux with the wall superheat for the microstructured etched surface at G =100 kg/m$^2$s.

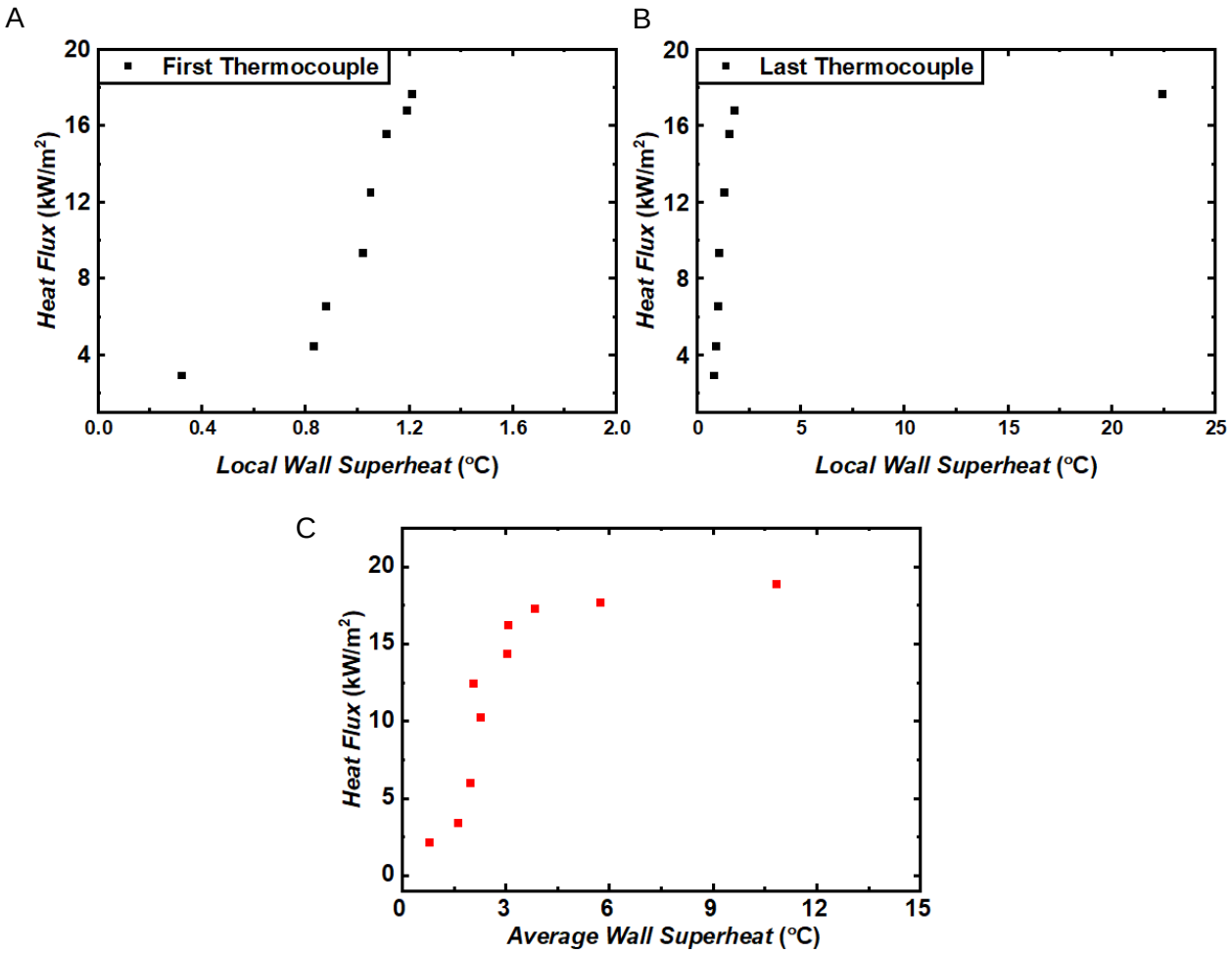


**Figure S2**. Boiling Curves at A) first thermocouple, B) last thermocouple and C) across the test-section at G =100 kg/m$^2$s.

**S8. Cavity Size**

Cavities on the surface are a prerequisite for initiation of boiling, and a few researchers have proposed relationships to quantity the dependence of various operational parameters on cavity size range. We utilize a relationship used by prior researchers[4, 5] to estimate the cavity size.[6]

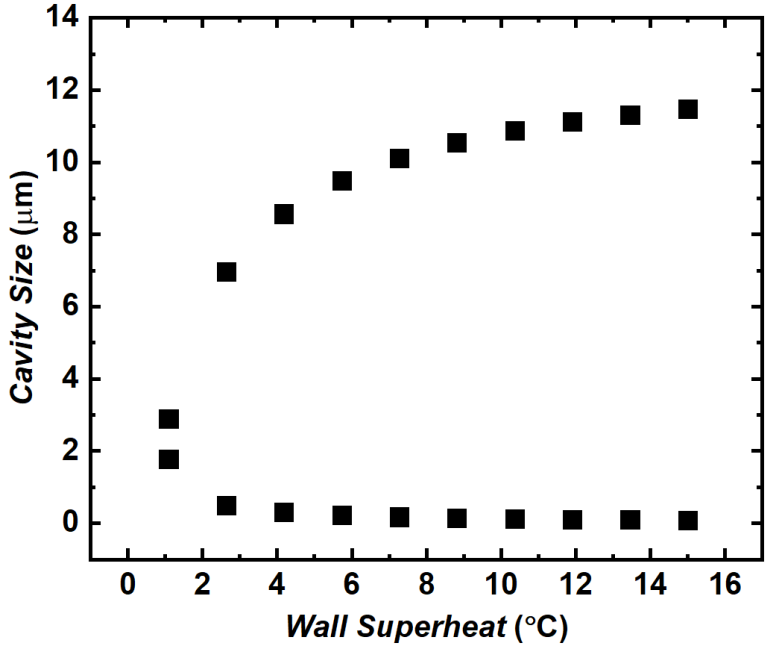


**Figure S3**. Active nucleation site radii range vs Wall superheat for 3.048 mm channel.

Figure S3 plots this variation over a range of wall superheat and the active nucleation size range is observed to be between 0.08-12 μm. The SEM images of the fabricated structures show an average cavity size of 5 μm for the etched surface which falls within this desirable range, while the cavity size for the nanostructured boehmite surface is 45 nm which lies below the estimated minimum radius. This explains the apparent negligible effect of additional cavities introduced through the fabricated nanostructured structure for flow boiling in our study.

**S9. Flow Regime Map**

A flow regime map based on transition vapor qualities is used in this study, with isolated bubble (IB), coalescing bubble (CB) and annular flow (A), being the three regimes encountered.[7] In this map, traditional flow regimes like bubble and slug-plug fall under the IB regime while slug and churn flow fall under the coalescing bubble regime. The transitions proposed are as follows:

$$X_{IB/CB} = 0.36(Co^{0.2})(\frac{\mu_v}{\mu_l})^{0.65}(\frac{\rho_v}{\rho_l})^{0.9}{Re_v}^{0.8}Bo^{0.25}{We_l}^{-0.91} \quad \text{(S5)}$$

$$X_{CB/A} = 0.047(Co^{0.05})(\frac{\mu_v}{\mu_l})^{0.7}(\frac{\rho_v}{\rho_l})^{0.6}{Re_v}^{0.8}{We_l}^{-0.91} \quad \text{(S6)}$$

where vapor Reynold's number $Re_v$, Boiling number Bo, liquid Weber number $We_l$ and Confinement number Co are defined as:

$$Re_v = \frac{GD}{\mu_v} \quad \text{(S7)}$$

$$Bo = \frac{q"}{Gh_{fg}} \quad \text{(S8)}$$

$$We_l = \frac{G^2 D}{\sigma \rho_l} \quad \text{(S9)}$$

$$Co = \frac{1}{D}\sqrt{\frac{\sigma}{g(\rho_l - \rho_v)}} \quad \text{(S10)}$$

Isolated bubble to coalescing bubble transition occurring at low vapor qualities, corresponding to about 0.05 at the highest mass flux case considered in this study G=300 kg/m$^2$s. As expected, an increase in mass flux leads to a decrease in the coalescing bubble to annular flow regime vapor quality transition.

## S10. Contact Angle Measurements

Contact angles for the fabricated microstructured and nanostructured surfaces are measured with R134a as the working fluid.

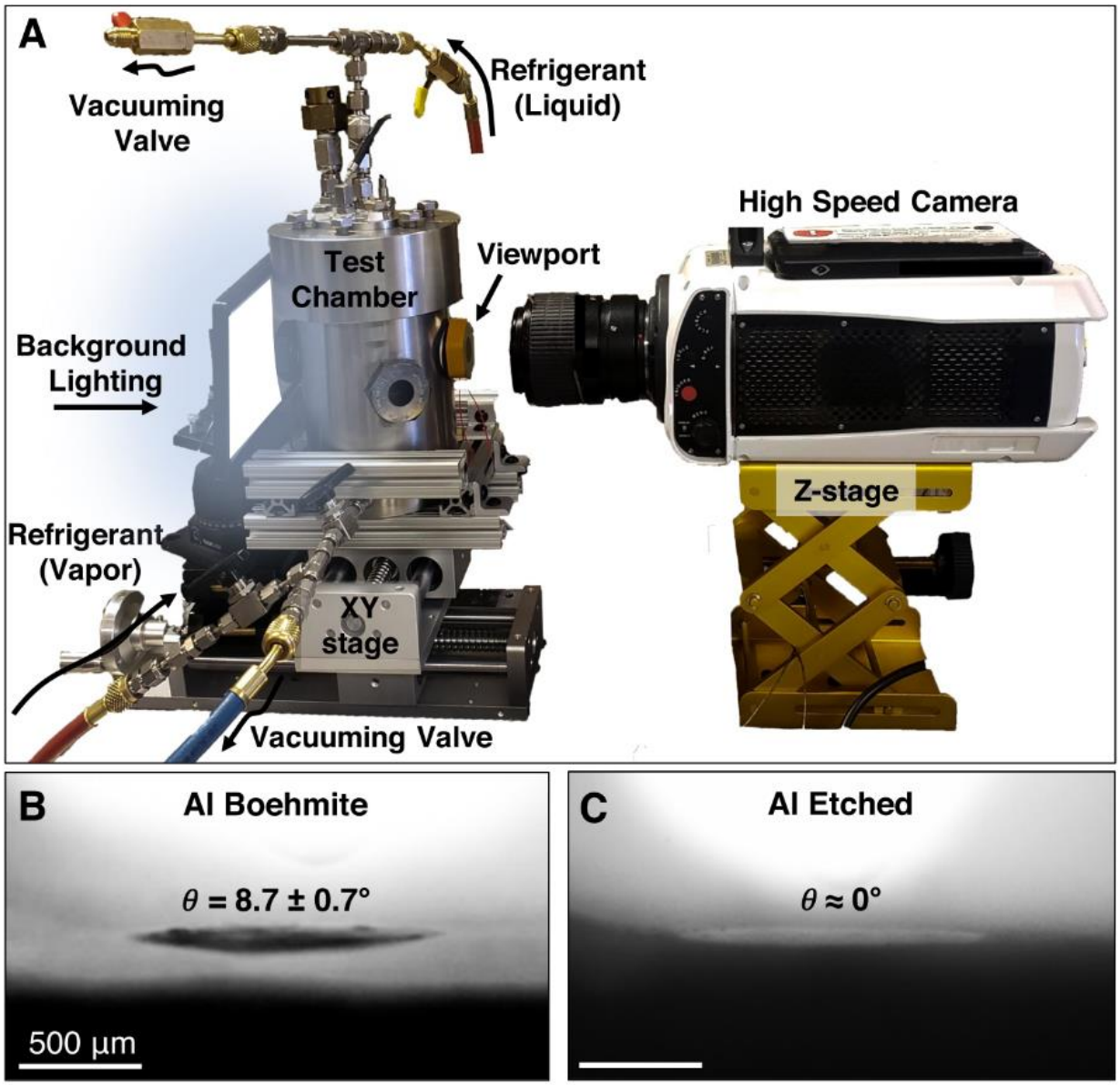


**Figure S4.** (A) Experimental facility to measure refrigerant contact angle, (B, C) Measurements for Al Boehmite and Al Etched using R-134a as the working fluid, showing nearly 0 ° contact angle (thin-film) for microstructured etched Al. Images were captured with a Phantom high-speed camera at 1500 FPS.

**S11. Flow Regime Analysis: Liquid Film Thickness and Turbulence**

Flow regimes at the exit of the test-section are recorded with a high-speed camera, and the average liquid thickness profile is calculated with the ImageJ software. Once the recorded image is inserted into the software, the image if first converted to 8-bit mode following which the auto-threshold option is enabled to represent the dark regions in the image – which correspond to liquid – with 0 and white regions in the image – which correspond to vapor – with 255 (Figure S9). On analyzing the histogram of distributed values, the area occupied by each phase in $pixel^2$ is obtained. A scaling factor from pixel to mm is then arrived at with prior knowledge of the outer diameter of the glass visualization section. The area occupied by the liquid film is then divided by the number of pixels in the X-direction to obtain the average film thickness in pixels. Using the derived scaling factor, this value is converted to mm to get the final liquid film thickness for stratified flow. For G = 102 $kg/m^2s$ and q = 9 $kW/m^2$, this leads to the etched Al surface displaying a 0.5 mm lower average film thickness in the stratified flow regime.

For the annular flow regime, a high degree of turbulence made it difficult to measure an average liquid film thickness. We modify our method highlighted above for liquid film thickness to determine the degree of turbulence using ImageJ. The greyscale images are converted to binary images by setting an optimum threshold pixel value to get maximum contrast between the refrigerant film and background lighting. This optimum threshold pixel value results in a film thickness variation of approximately ± 0.01 mm. Figure S5 demonstrates the variation in liquid film thickness for the top and bottom films in annular flow for G = 306 $kg/m^2s$ and q = 43 $kW/m^2$.

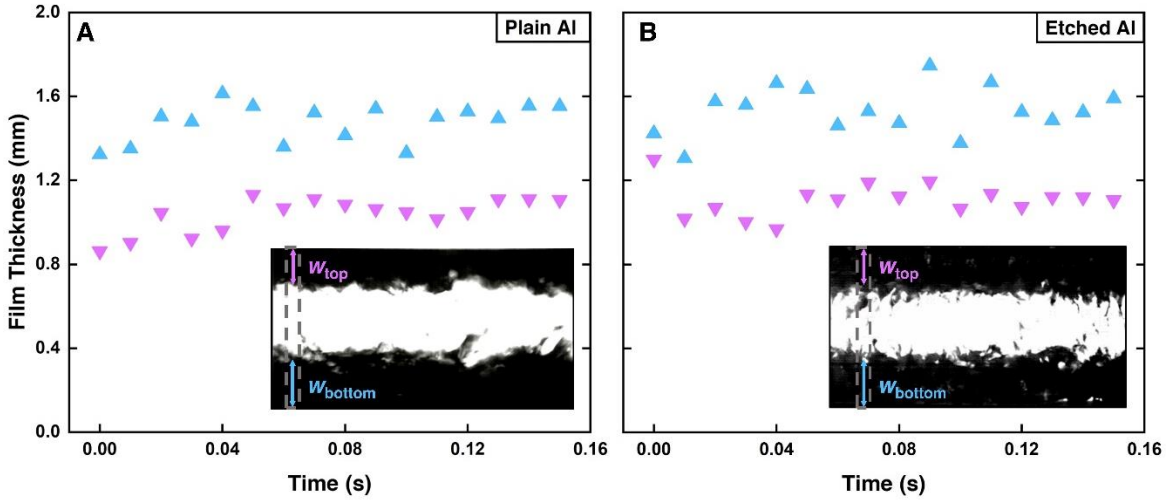


**Figure S5.** Film thickness variation for a sliced portion of image during annular flow for A) plain Al and B) etched Al, as a function of time

Table S4 showcases the top and bottom film thickness standard deviations.

**Table S4.** Standard deviations of top and bottom film thickness at G = 306 kg/m$^2$s and q = 43 kW/m$^2$

| Surface | Film Location | Standard Deviation (mm) |
|---|---|---|
| Plain | Top | 0.0825 |
| | Bottom | 0.0915 |
| Microstructured Etched | Top | 0.0937 |
| | Bottom | 0.1141 |

The microstructured etched surface exhibits larger standard deviation in film thickness for both the top and bottom films when compared to the plain surface and thus demonstrates a higher degree of turbulence. In addition, the heat transfer coefficients were observed to be generally higher at the bottom thermocouple when compared to the top. This can be attributed to the increased turbulence of the bottom liquid layer during annular flow.

**References**


1. Friedel, L., Improved Friction Pressure Drop correlation for Horizontal and Vertical Two-phase Pipe Flow. *Proc. of European Two-Phase Flow Group Meet.* **1979**, 18 (7), 485-491
2. Chisholm, D., Two-phase Flow in Pipelines and Heat Exchangers. In *Heat Transfer Eng.*; Taylor and Francis, **1983**; pp 48-57
3. Taler, D.; Taler, J. In *Simple heat transfer correlations for turbulent tube flow*, E3S Web of conferences, EDP Sciences: 2017; p 02008.
4. Yang, F.; Li, W.; Dai, X.; Li, C., Flow Boiling Heat Transfer of HFE-7000 in Nanowire-coated Microchannels. *Appl. Therm. Eng.* **2016,** *93*, 260-268.
5. Li, D.; Wu, G.; Wang, W.; Wang, Y.; Liu, D.; Zhang, D.; Chen, Y.; Peterson, G.; Yang, R., Enhancing Flow Boiling Heat Transfer in Microchannels for Thermal Management with Monolithically-integrated Silicon Nanowires. *Nano Lett.* **2012,** *12* (7), 3385-3390.
6. Hsu, Y., On The Size Range of Active Nucleation Cavities on a Heating Surface. *J. Heat Transfer* **1962,** *84*, 207.
7. Ong, C. L.; Thome, J., Macro-to-microchannel Transition in Two-phase Flow: Part 1–Two-phase Flow Patterns and Film Thickness Measurements. *Exp. Therm Fluid Sci.* **2011,** *35* (1), 37-47.